

Causal explanations of outliers in systems with lagged time-dependencies

Philipp Alexander Schwarz*
 AMS-Osram
 University of Hamburg

Johannes Oberpriller
 AMS-Osram

Sven Klaassen
 University of Hamburg
 Economic AI

Abstract

Root-cause analysis in controlled time dependent systems poses a major challenge in applications. Especially energy systems are difficult to handle as they exhibit instantaneous as well as delayed effects and if equipped with storage, do have a memory. In this paper we adapt the causal root-cause analysis method of Budhathoki et al. [2022] to general time-dependent systems, as it can be regarded as a strictly causal definition of the term “root-cause”. Particularly, we discuss two truncation approaches to handle the infinite dependency graphs present in time-dependent systems. While one leaves the causal mechanisms intact, the other approximates the mechanisms at the start nodes. The effectiveness of the different approaches is benchmarked using a challenging data generation process inspired by a problem in factory energy management: the avoidance of peaks in the power consumption. We show that given enough lags our extension is able to localize the root-causes in the feature and time domain. Further the effect of mechanism approximation is discussed.

Keywords: Causal Inference, Machine Learning, Root Cause Analysis, Energy Peaks

1 Introduction

Explaining the behavior of dynamical systems poses a major challenge in contemporary research. In recent years data-driven methods have fostered the analysis and optimization of complex systems in various research branches, like earth sciences [Runge et al., 2019a,b], energy management [Guo et al., 2024] and epidemiology [Borges et al., 2025]. Particularly, the problem of identifying causes of anomalies in such systems has gained major attraction. While most of this attention is coming from cloud-computing [Wang et al., 2023, Liu et al., 2021, Lin et al., 2024, Ikram et al., 2022] the methodology also finds application areas like healthcare Strobl [2024]. In general, *Root Cause Analysis (RCA)* tries to locate the sources of outlier events with the goal to use the resulting explanations to take actions that steer the system in question back to a normal state, or to avoid similar anomalies in the future. We follow the view of Budhathoki et al. [2022] that in these cases explanations should be derived from causal relations affecting the target variable. That is, the applied methodology should be based on counterfactual reasoning. For a review of the three main methodology groups, namely correlation-based, causal and hybrid approaches, we refer to Dawoud and Talupula [2025].

Further we argue that complex systems may exhibit lagged time-dependencies that make RCA especially challenging:

1. The system may contain variables that have an instantaneous and others that have a delayed effect on the target, a property that prohibits simplification of time-series data through coarse aggregations [Runge, 2018].
2. The systems target variable may be controlled or self-regulating which implies that anomalies are seldom rooted in a single cause. That is, outlier behavior of a subsystem may only propagate to the systems target if the control mechanism is also faulty.
3. The system may have a memory which implies potential long-ranging effects on its target.

In order to deal with these challenges we adopt the *causal structur-based root cause analysis (CRCA)* method from Budhathoki et al. [2022] to lagged time-dependencies. This choice is deliberate and in contrast to existing methods that deal with time-series data. Lin et al. [2024] and Wang et al. [2023], for example, rely on weaker forms of causality, that is Granger causality, but employ advanced machine learning techniques to estimate the causal structure. Our rational is that CRCA can be viewed as an attempt to formalize the notion of root-causes in the framework of structural causal models. In this sense the present study can be seen as an evaluation of the basic definition of root causes in time dependent domains.

As an example and benchmark serves a *data-generating process (DGP)* modeling the electrical system of a hypothetical manufacturing plant. It consists of energy consumers (e.g. tool parks), stores (e.g. battery) and producers, and is connected to the public grid. The power draw from the public grid is regulated not to exceed a certain limit, such that consumption peaks exceeding this limit can be regarded as anomalies. Note that, a machine may increase its power consumption only with a delay of several minutes after the start of production, whereas the loading and unloading of a battery storage affects the power draw almost immediately. A behavior that is represented by the DGP. In summary the studied DGP exhibits the challenges mentioned before.

2 Methodology

In this section we introduce the basic causal setting and adapt the CRCA method to it. Particularly, regarding causality, we rely on the framework of Pearl [2022], and make use of *causal structural models (SCMs)* as defined in [Peters, 2017]. Note that time series have been studied before in this context (e.g. [Runge, 2018]). We use the notation $\mathbb{Z}_{\leq t} := \{s \in \mathbb{Z} \mid s \leq t\}$ for the set of integers lower or equal to t . Let

$X_t := (X_t^1, \dots, X_t^n)$ be a discrete-time multivariate process that propagates in time according to the causal structural model

$$X_t^i := f^i(\text{Pa}_t^i, N_t^i) \quad (1)$$

where N_t^i denote the noise variables and $\text{Pa}_t^i \subset \{X_s^i \mid s \in \mathbb{Z}_{\leq t}, i = 1, \dots, n\} \setminus \{X_t^i\}$ the sets of parent dependencies. We suppose that the parent dependencies Pa_t^i are finite, acyclic and do not change with time. For fixed i let the noise terms N_t^i be time independent and identical distributed, such that $X_t^i = f^i(\text{Pa}_t^i, N^i)$ holds with $N^i := N_0^i$. Under these assumptions we can summarize the infinite time dependency graph of X_t as shown in Figure 1. Further we assume the components of the noise vector $N := (N^1, \dots, N^n)$ to be jointly independent in accordance to the definition the SCM. The lower case notation (e.g. n_t^i and pa_t^i) is used to denote realizations of the matching capitalized random variable, or set of random variables (e.g. N_t^i and Pa_t^i).

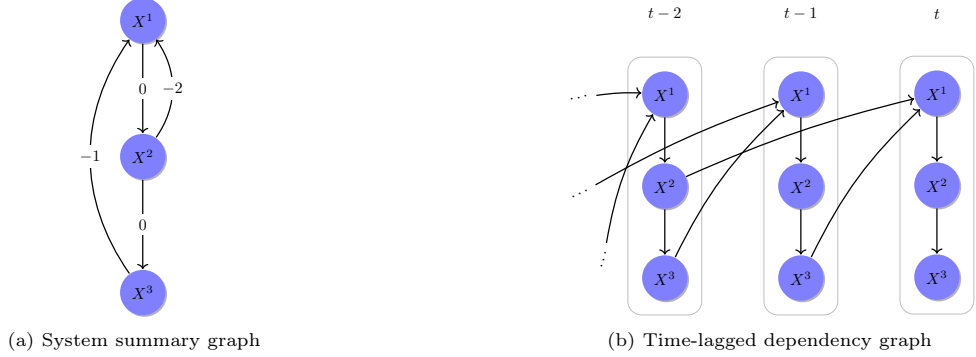


Figure 1: Dependencies of an exemplary system with $X_t^1 := f_1(X_{t-2}^2, X_{t-1}^3 \mid N^1)$, $X_t^2 := f_2(X_t^1 \mid N^2)$ and $X_t^3 := f_3(X_t^2 \mid N^3)$.

We follow Budhathoki et al. [2022] and view X_t^n as the systems target, for which we want to explain anomalous behavior. That is, for which we want to localize root-causes among the individual time series X_t^1, \dots, X_t^n . To apply the CRCA methodology, it is necessary to limit the search to a certain time interval $[t-L, t]$ where $L \in \mathbb{Z}_{\geq 0}$ denotes the maximum time-lag considered. Choosing a finite maximum lag narrows the root-cause identification down to the more immediate past excluding very long range effects. Especially in systems with a memory choosing L is a tradeoff between relevance, accuracy and computational time. Let

$$\text{Pa}_t^i(l) := \{X_s^j \mid s \in \mathbb{Z}_{\leq t-l}, j = 1, \dots, n\} \cap \text{Pa}_t^i$$

and respectively

$$\text{Pa}_t(l) := \text{Pa}_t^1(l) \cup \dots \cup \text{Pa}_t^n(l)$$

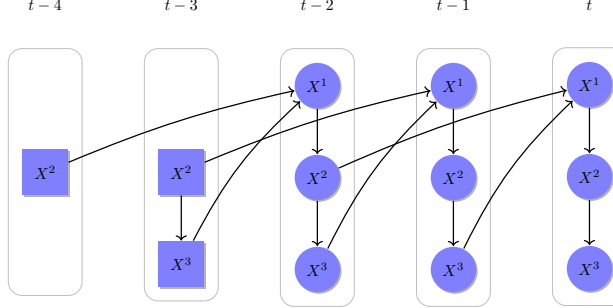


Figure 2: Unfolding and truncation of example graph shown in Figure 1a with $L = 2$: The rectangular nodes represent the dangling parents $\text{Pa}_{[t-2, t]}(3) = \{X_{t-4}^2, X_{t-3}^2, X_{t-3}^3\}$ on which we condition in the truncation model whereas the noise terms $N_{[t-L, t]} = \{N_{t-2}, N_{t-1}, N_t\}$ of the circular nodes are assessed in the attribution analysis. In the non-truncated case the mechanisms and noise distributions of the dangling nodes are adapted the remaining dependencies (e.g. $X_{t-3}^2 \rightarrow X_{t-3}^3$ remains while X_{t-3}^2 has no more parents) and then also employed for the attribution analysis.

denote the parent dependencies of X_t^i and X_t with minimum time-lag $l > 0$. Through a recursive argument one can show that X_t^n can be written as a function F_L of noise terms $N_{[t-L, t]} := (N_{t-L}, \dots, N_t)$ up to lag L and parent dependencies $\text{Pa}_{[t-L, t]}(L+1) := \bigcup_{l=0}^L \text{Pa}_{t-l}(L-l+1)$ that exceed L :

$$X_t^n = F_L \left(\text{Pa}_{[t-L, t]}(L+1), N_{[t-L, t]} \right)$$

This procedure can be seen as an L -times unfolding of the summary graph of the system (see Figure 2), followed by a truncation at the dangling parents $\text{Pa}_{[t-L, t]}(L+1)$ and puts us in a position to apply CRCA up to nodes of lag L . The basic idea of CRCA is that extreme noise realizations are at fault for an anomaly. Thus, the question asked to locate the root-causes is: would an anomaly still be probable if certain nodes had received normal noise values according to their distributions instead of the observed? More precisely we suppose that at time t a system anomaly x_t^n was observed with noises $n_{[t-L, t]}$ and dangling parents $\text{pa}_{[t-L, t]}(L+1)$. Then the attributions of nodes X_{t-l}^i with $l = 1, \dots, L$ and $i = 1, \dots, n$ are calculated by probing the structural model

$$n_L \mapsto F_L \left(\text{pa}_{[t-L, t]}(L+1), n_L \right), \quad (2)$$

combining the observed noise terms $n_{[t-L, t]}$ with randomly sampled $n_L \sim N_{[t-L, t]}$. We refer to this SCM as the *truncated* lag L model. Note that the described truncation procedure leads to an equal assessment of the lags of X_t^i as the generating mechanism f^i is kept intact up to the max lag L , by conditioning on the observed dangling parents $\text{pa}_{[t-L, t]}(L+1)$. This stands in contrast to the *non-truncated* lag L model for which the mechanisms f^j related to the dangling variables $X_{t-l}^j \in \text{Pa}_{[t-L, t]}(L+1)$ modified to fit the

remaining parents

$$X_{t-l}^j = h_l^j \left(\text{Pa}_{[t-L, t]}(L+1) \cap \text{Pa}_{t-l}^j, \hat{N}_{t-l}^j \right)$$

approximating the dependency structure of the actual structural model. As indicated by the notation this approximation may have an effect on the noise distribution. Again using a recursive argument on h_l^j we obtain the corresponding SCM

$$(n_D, n_L) \mapsto F_L(H_L(n_D), n_L) \quad (3)$$

where H_L maps the noises $\hat{N}_{[t-l, t]}(L+1)$ of the dangling parents under the changed functional model to their values:

$$\text{Pa}_{[t-L, t]}(L+1) = H_L \left(\hat{N}_{[t-L, t]}(L+1) \right)$$

This procedure approximates the causal mechanisms and noise distributions of the initial dependencies in the unfolded graph. In the attribution calculation the noise terms of the dangling parents are then considered in addition to the noises up to lag L . With this the non-truncated lag L model stands in complexity and in the number of attributable nodes between the truncated lag L and the truncated lag L_D model where L_D is the maximum lag among the variables $\text{Pa}_{[t-L, t]}(L+1)$. We investigate the performance of both variations in the application example.

For completeness, we recapture definition of the CRCA attributions introduced in Budhathoki et al. [2022] and apply it to the above setting. Let $g : \mathcal{X} \rightarrow \mathbb{R}$ be an anomaly score, like the z-score, and let E_t be the outlier event $E_t := \{g(X_t^n) \geq g(x_t^n)\}$ then the corresponding *information theoretic calibration (IT-Score)* of g is defined as $S(x_t^n) := -\log \Pr(E_t)$. Further, let \mathcal{U} denote set of tuples (i, l) indexing the nodes X_{t-l}^i and their corresponding noise values N_{t-l}^i . Note that for the truncated lag L model we have $\mathcal{U} = \{1, \dots, n\} \times \{0, 1, \dots, L\}$. In case of the non-truncated model \mathcal{U} additionally includes indices for the dangling nodes. For a subset $\mathcal{I} \subset \mathcal{U}$ we define

$$q_t(\mathcal{I}) := \Pr(E_t \mid N_{t-l}^i = n_{t-l}^i \forall (i, l) \in \mathcal{U} \setminus \mathcal{I})$$

to be the probability of the outlier event E_t when randomizing the noises of the nodes $(i, l) \in \mathcal{I}$ according to their distributions N_{t-l}^i and keeping the other nodes fixed to the observed values n_{t-l}^i . To evaluate these probabilities the structural models (2) and (3) are used. Further, for a node $u \in \mathcal{U}$ let

$$C_t(u \mid \mathcal{I}) := \log \frac{q_t(\mathcal{I})}{q_t(\mathcal{I} \cup \{u\})}$$

be the contribution of u under randomization of $\mathcal{I} \subset \mathcal{U} \setminus \{u\}$. Then the attribution of node u to the anomaly x_t^n is then defined as

$$\phi_t(u) := \frac{1}{|\mathcal{U}|} \sum_{\mathcal{I} \subset \mathcal{U} \setminus \{u\}} \left(\frac{|\mathcal{U}| - 1}{|\mathcal{I}|} \right)^{-1} C_t(u | \mathcal{I})$$

using Shapley values [Shapley, 1952] to factor out the dependence of C_t on specific index sets. The IT-Score decomposes into the attributions as follows:

$$S(x_t^n) = \sum_{u \in \mathcal{U}} \phi_t(u) \quad (4)$$

With this method we do not only obtain the nodes at fault for an anomaly but also information that aids the localization in time.

To apply the method it is required that the noise terms n_t^i can be calculated from the observed values x_t^i and pa_t^i through inversion of $x_t^i = f^i(\text{pa}_t^i, n_t^i)$. Further when estimating f^i (or the distribution of N_t^i) the time-independence assumptions regarding the noise distributions ensure that the computational and memory requirements are not dependent on L . This also applies to the memory required for the sampling of noise terms to estimate q_t . However, the L -times unfolding increases the computational complexity to calculate ϕ_i from $n!$ to $(Ln)!$. We adapted the existing implementation in Sharma and Kiciman [2020], Blöbaum et al. [2024] with minimal changes, and thus do not make use of the mentioned independence assumptions. In particular, we estimate a functional causal model for each node and time lag.

3 Empirical Setting

In this section we describe the experimental setup to evaluate the time-lagged adaption of CRCA. Part of the contribution is a data-generating process that allows to inject defined root causes in the system. This allows to calculate the system propagation with and without injected root causes, and thus to evaluate CRCA.

3.1 DGP

The data generating process models the energy consumption of a hypothetical manufacturing plant. The plant is connected to an external Grid that serves as an unlimited power source. Further it consists of two tool parks TP_a and TP_b connected to the grid injection point. Each tool park is composed of several machines that draw power from the tool park connection point. That is, when switched on a machine consumes power according to its active profile. If production is finished the machine turns back to an idle state drawing power according to the idle profile. The active profile models a ramp-up phase followed by a phase of

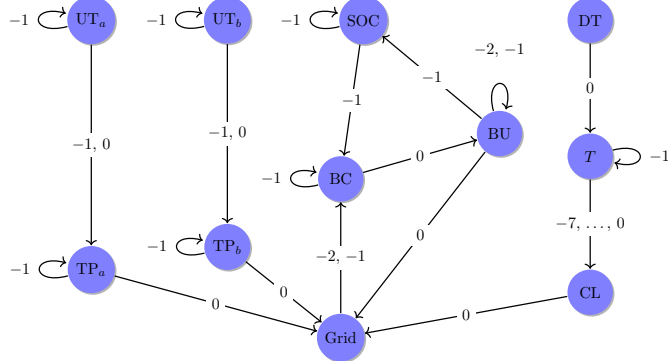


Figure 3: System summary graph of the DGP

high power draw and finally ends with a ramp-down. The machine specifics vary only between machines of different tool parks. The wait times between the arrival of work items are modeled to be exponentially distributed. Thereby the utilization level of the tool parks UT_a and UT_b tracks the share of active machines. Moreover, in our example plant it is required to keep the production environment at a certain temperature level. Thus, we model the cooling power CL of the fab to be dependent on the outside temperature T . The cooling equipment is switched on if the average temperature of the last three minutes was over the threshold of $19^{\circ}C$ and turned off if it drops below $18^{\circ}C$. The resulting power draw from the grid junction point is time-delayed by five minutes and proportional to the temperature. The temperature T is dependent on the current time of the day DT as real weather data is used. The overall consumption is regulated using an on-site battery system. Again we use a two-point battery controller BC that signals the battery to remain idle, load or unload, depending on the average draw from the grid over the last two minutes. That is, if the average power draw is above $1400kW$ the battery immediately starts to unload and continues to do so until $1100kW$ are reached. Thereby the controller maintains a state of charge SOC between 70% and 90% . Thus, if SOC drops below 70% the battery is loaded independently of the average power draw from the grid. To recapitulate, the overall grid consumption is defined as the sum of the tool park, the cooling system, and battery consumption in addition to a normal distributed noise to include unobserved consumers or producers. Variations in the machine, cooling system and battery consumption are also incorporated using an additive noise. In this setting we regard peaks in the grid consumption that exceed $1500kW$ as anomalies if they have a width of at least two time steps measured from both turning points. The described DGP produces time series data that is aggregated on a minute level for each of the described features. Further it allows injecting anomalies in each major component as discussed in Section 3.2.

The summary graph of the system and exemplary output is shown in Figure 3 and Figure 4. Note that the used dependency graph only approximates the simulation, since individual machine states are not included but approximated through the derived variables UT_a and UT_b . Moreover, the relation of temperature T and

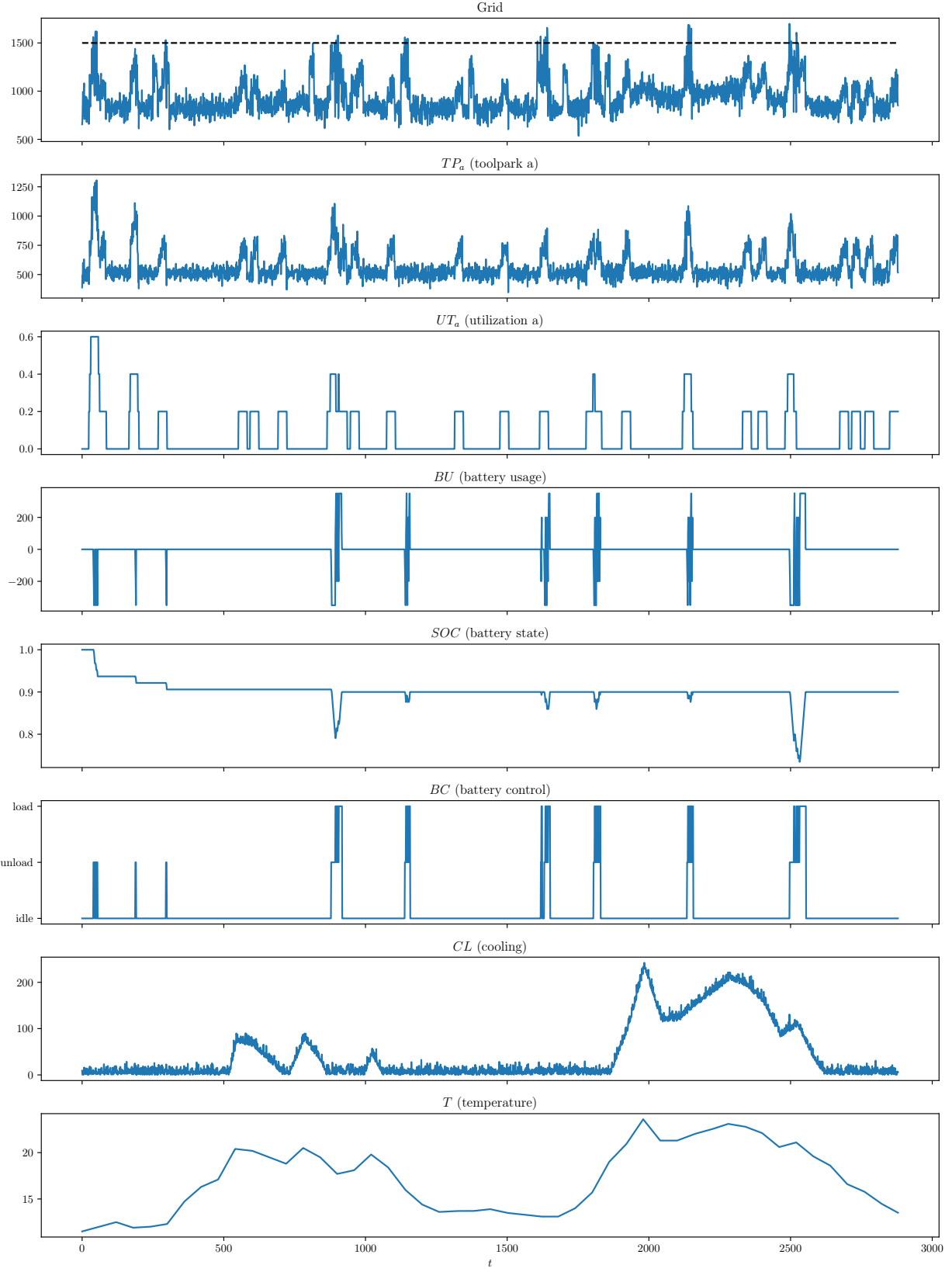


Figure 4: Exemplary DGP output: The dotted horizontal line in the Grid graph signifies the peak limit

daytime DT is implicit since real-world data is used for these nodes. Put differently, the simulation does not directly fit the functional form of Equation 1 given the dependency graph in Figure 3. It rather represents a reasonable approximation, as required in many real application settings.

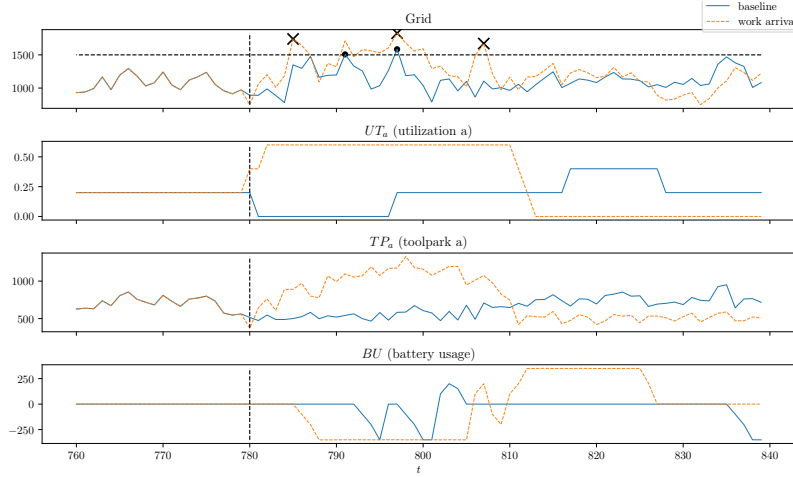
3.2 Injections

In this section we describe the method used to inject deviations that lead to energy peaks with assignable root-causes. In general two simulation runs with the same initial condition and random seeding are compared. While the first run is not modified and represents the baseline, the second run diverges from the first through one of the following injections:

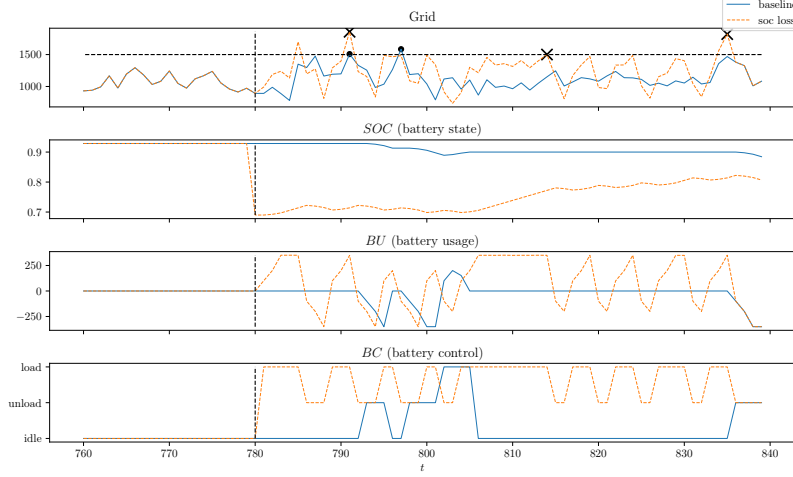
1. *temperature surge*: The temperature is set to a high value ($T = 31^{\circ}C$) for an extended time period ($\Delta t = 10$), directly affecting T . In application such a scenario may happen due to sensor failures, e.g. the sensors being blocked by an object, or faulty readouts.
2. *cooling surge*: The required cooling power is set to high value ($CL = 265kW$) for an extended time period ($\Delta t = 10$), directly affecting CL . In application this scenario may occur due to control failures. For example suppose that an individual cooling machine failed during startup. Thus, an additional machine is immediately started to compensate the required cooling power. But the first machine might still draw a substantial amount of power until it is shut down.
3. *cooling scale*: The scaling factor used to calculate the required cooling power given the temperature is increased ($75 \frac{kW}{^{\circ}C}$) compared to the normal setting ($60 \frac{kW}{^{\circ}C}$) for an extended time period ($\Delta t = 10$), directly affecting the calculation of CL . In an application setting the internal control target, that regulates the individual cooling machines might be set to a high value due to sensor failures or situations of high humidity might lead to a higher consumption of the cooling equipment.
4. *bat fail*: The battery output is set to zero ($BU = 0kW$) for an extended time period ($\Delta t = 15$), directly affecting BU . This simulates a failure in the battery system in which the battery does not produce any output independently of the controller.
5. *soc loss*: The state of charge of the battery is immediately set to a low value ($SOC = 0.69$) directly affecting SOC and causing the battery controller to load the battery until it is in normal SOC range. This injection has long-term effects on the system propagation, as it changes the load cycles of the battery. Loosing a large amount of charge in a real-world application would indicate a severe failure of the battery system. We regard this as a rather uncommon but interesting case as it showcases typical behavior of systems with memory.

6. *work arrival*: Three work items arrive at tool park a within three minutes affecting UT_a . This causes several machines to be activated in a short time. In applications such a scenario may happen after work breaks or during a shift handover and may lead to peaks which would be avoidable with better synchronization.
7. *grid noise*: For an extended period of time ($\Delta t = 10$) the normal distributed noise variable affecting the Grid node is replaced by a normal distributed variable with higher standard deviation. The high value is given by $\sigma = 550kW$ compared to the normal setting with $\sigma = 30kW$. This behavior mimics the activation of additional consumers or producers in the plant that are not explicitly tracked through any of the tool parks. This injection is a standard non-time-dependent system alteration similar to the alterations used by Budhathoki et al. [2022].

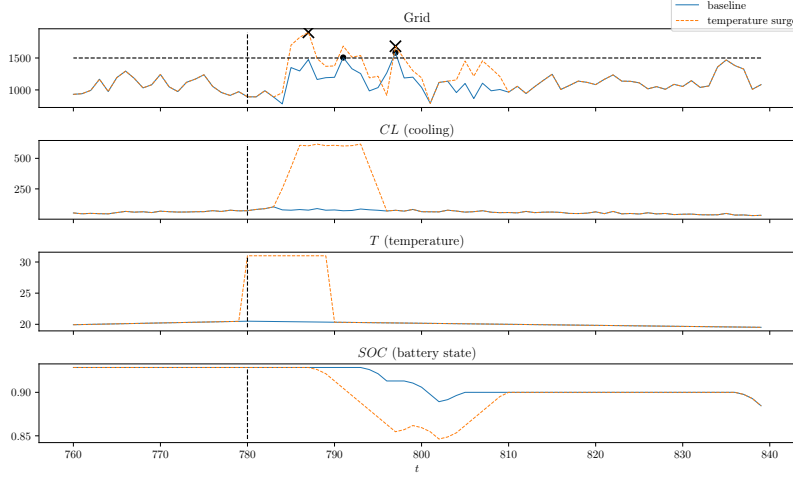
In the second run the selected injection is activated at time t_I and remains Δ_I minutes active as specified. In particular t_I is chosen such that the initial conditions of the simulation have faded off. Now if a peak occurs in the second simulation run that has not been present in the baseline simulation or is of higher magnitude than a peak in the baseline, this peak is attributed to the node that is affected by the injection. All other peaks are rejected. We restrict our attention to peaks that emerge in the time interval $[t_I, t_I + \tau]$ after the injection start with $\tau > 0$. Thus, attributable peaks may appear during an activated injection or afterward. Figure 5 visualizes the effect of the *soc loss*, *work arrival* and *temperature surge* injections. As it can be seen by the third injection peak in Figure 5a the cause effect chain spreads out through time and multiple system nodes. The higher tool park utilization caused the battery controller to unload and later to load the battery again resulting in the peak. Further, Figure 5c showcases a time-delayed cause effect chain where the system recovers smoothly from injection transitioning back into its baseline state after some time. This stays in contrast to the far-reaching *soc loss* injection that causes peaks with great delay as shown in Figure 5b.



(a) work arrival



(b) soc loss



(c) temperature surge

Figure 5: Exemplary system propagation with (orange) and without (blue) injection. The most relevant system nodes are shown. The injection starts at the vertical dotted line and the peak limit is given by the horizontal dotted line. Peaks caused by the injection (marked with X) are determined by comparison with the baseline.

3.3 Benchmark

In this section we describe our benchmark procedure. We draw 40 baseline samples with different seeding from the DGP simulating the same time period $[t_s, t_I + \tau]$ starting at time t_s . For each of the injections described in Section 3.2 the baseline simulations are repeated using the same seeding but activating the injection at time t_I . Comparing the injected simulation runs with the corresponding baseline samples in the time interval $[t_I, t_I + \tau]$ leads to the attributable peaks shown in Table 1. For some injections the number of generated peaks is lower than the number of samples. Indeed, in some cases the battery is able to stabilize the system mitigating the injection. The *bat fail* injection disables this mitigation measure, which in the first place does not cause any extraordinary power consumption by itself. It rather reveals anomalies previously mitigated. This means that in controlled, self-stabilizing systems an outlier is not likely to be explained by a singular root-cause. Figure 6 visualizes the distribution of the attributable peaks in time. The *soc loss* and *work arrival* peaks are more time delayed compared to the peaks generated through the *grid noise* or *cooling surge* injections.

To train the SCM we draw three samples from the DGP simulating a whole month starting from t_s . While for each sample a different seed is used the temperature profile remains the same. For a given maximum lag L we unfold the system summary graph shown in Figure 3 as described in Section 2. Then causal mechanisms are assigned according to the dependencies of the unfolded graph. The difference between the truncated and non-truncated model is that in the latter case the dependency graph includes the dangling nodes with modified parent dependencies, whereas the former truncates at lag L leaving the overall dependency structure intact. At the battery control node BC we assign the actual control mechanisms. This is in line with the application perspective, where it can be assumed that the control logic is known. This also means that f^{BC} is not dependent on a noise variable and thus does not get any attributions. For the other nodes we rely on the auto assign heuristic implemented in the dowhy package [Blöbaum et al., 2024, Sharma and Kiciman, 2020]. Note that from the application perspective the system would admit adding further physical constraints to the model. For example, the values of Grid and its direct parents TP_a , TP_b , BU and CL can be thought

Table 1: Number of attributable peaks per injection.

injection	affected nodes	peaks
bat fail	BU (battery usage)	10
cooling scale	CL (cooling)	22
cooling surge	CL (cooling)	10
grid noise	Grid	30
soc loss	SOC (battery state)	96
temperature surge	T (temperature)	69
work arrival	UT_a (utilization a)	83

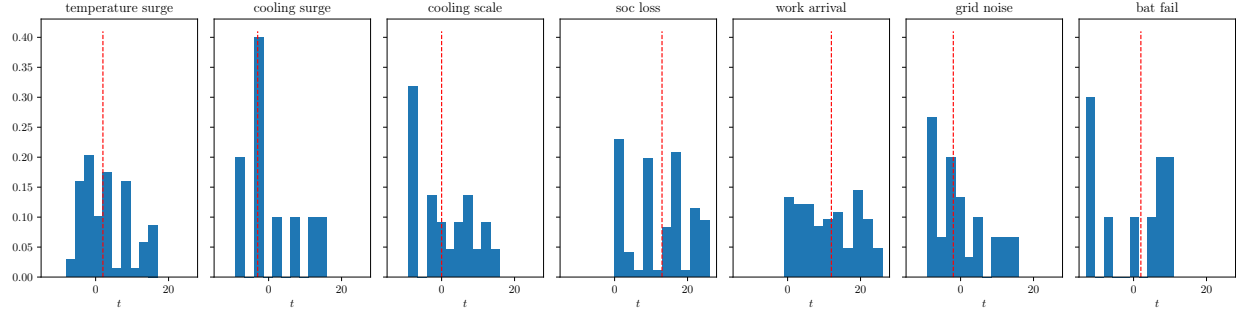


Figure 6: Distribution of attributable peaks in time per injection: The time axis is relative to the injection end and the median time delay relative to the injection end is marked by the red dotted line.

of as time synchronous power meter measurements at their respective grid junction points. Thus, if the measurements have the same unit, the functional model f^{Grid} has to be linear with coefficients being equal to one. The trained model is used to calculate attributions for each peak generated by an injection.

Further, we compare the CRCA models to a simple peak attribution heuristic (Algorithm 1). The idea behind the heuristic algorithm is to explain the increase (decrease) of a node i during the build-up of the peak through increases (decreases) of its parents in the same period while assuming a linear structural model with a dependency tree. The residual part of the increase is then attributed to the node i itself. To make the different features comparable the coefficients of the linear mechanisms are used to reweight the attributions. If we disregard the SOC, BC and DT nodes as well as the time-lagged dependencies in the system summary

Algorithm 1: Heuristic (residual peak attributions)

Data: target limit y , linear coefficients $w_{i,j}$ of parents i on the children j , data x with peak at $x_t^n > y$,

Result: attributions Φ_i of the nodes $i = 1, \dots, n$
 calculate the time lag $s \leftarrow \min\{l \in \mathbb{N} \mid x_{t-l}^n > y \geq x_{t-l-1}^n\}$ of the first overshoot before the peak;

for all nodes i **do**

- $\delta^i \leftarrow x_t^n - x_{t-s}^n$ calculate the peak increase;
- find the shortest path $(i, j_1, j_2, \dots, j_k, n)$ from i to n in the dependency tree;
- $\lambda^i \leftarrow w_{i,j_1} w_{j_1,j_2} \dots w_{j_k,n}$;
- reweight the increase $\delta^i \leftarrow \delta^i \lambda^i$;

end

for all nodes i **do**

- determine the set of parent nodes Pa_i of i ;
- $\Phi_i \leftarrow \delta^i - \sum_{j \in \text{Pa}_i} \delta^j$;

end

graph (Figure 3) the remaining dependency tree can be plausibly approximated through linear mechanisms. As argued above the mechanism f^{Grid} is linear in its direct parents with coefficients equal to one. The remaining coefficients are regressed from data. This, coefficients are interpreted as average conversion factors for the increases, e.g. in case of $UT_a \rightarrow TP_a$ the related coefficient w_{UT_a, TP_a} is understood as the average

increase of cooling power per increase of the utilization.

3.4 Evaluation

Denote with \mathcal{P}_I the set of peaks caused by injection I and let $c_I \in \{1, \dots, n\}$ be the node affected by I . For a peak $p \in \mathcal{P}_I$ at time t_p we aggregate the CRCA attributions of a particular lag L model in time to assess the feature localization capability. Particularly, we evaluate

$$\Phi_p(i) := \Phi_p(i, L) := \text{agg}_{l \in \mathcal{U}_i} \phi_{t_p}(i, l)$$

for different lag aggregations $\text{agg} \in \{\max, \sum\}$ to rank the graph nodes $i \in \{1, \dots, n\}$. Thereby $\mathcal{U}_i := \{l \mid (i, l) \in \mathcal{U}\}$ is defined as the set of available lags for node i given the lag L model. Then the hit rates

$$\text{HR}@k(I, L) := \frac{1}{|\mathcal{P}_I|} \sum_{p \in \mathcal{P}_I} \mathbb{1}[c_I \in \text{Rank}^k(p, L)]$$

given injection I are calculated, where $\text{Rank}^k(p, L)$ denotes the k highest ranking nodes with respect to the attributions $\Phi_p(1), \dots, \Phi_p(n)$. While the injection dependent hit rate reveals performance differences between the anomaly types, the independent hit rate $\text{HR}@k(L)$ is used to equate the overall performance. The peak heuristic attributions are evaluated accordingly without the prior aggregate over the time-lags.

To assess the time localization capability of the CRCA method we compute the predicted anomaly time

$$\hat{t}_I := t_p - \arg \max_{l \in \mathcal{U}_{c_I}} \phi_{t_p}(c_I, l)$$

as the peak time t_p minus the time lag of the targeted node c_I having the maximum attribution. Thus, we assume that the feature localization is known. Thereby we view the method to be successful if the predicted anomaly time lies in the interval $[t_I, t_I + \Delta_I]$ during which the injection I was active. Consequently, we use the following comparison function:

$$d(t_I, \hat{t}_I) := \begin{cases} 0, & \hat{t}_I \in [t_I, t_I + \Delta_I] \\ \hat{t}_I - (t_I + \Delta_I), & \text{otherwise} \end{cases}$$

4 Results

In this section we present the evaluation results, with the truncated model being evaluated for maximum lags $L = 1, \dots, 13$ and the non-truncated for $L = 1, \dots, 10$. We compare the feature localization capability of

the truncated and non-truncated models. Thereby, the peak heuristic serves as a semi-time-dependent lower bound. By construction, it is not to be expected that the heuristic can capture root causes with long time delays and thus should only be comparable to truncated models with low maximum lag. Further, we evaluate the time localization performance of the CRCA models. Lastly, the effect of the mechanism approximation in non-truncated models is discussed by examination of an example peak.

4.1 Feature Localization

As argued before, in regulated systems it is not likely that an outlier is produced by a singular cause. Accordingly, it cannot be expected that the injected root cause is always clearly distinguished from other potential root causes in terms of the calculated attributions. We rather argue that the injected root cause should at least be among the three highest ranking causes, which makes HR@3 the main metric to compare the different variations. Of course this depends on the number of available features. Table 2 gives an overview of the CRCA HR@3 results.

Table 2: HR@3 overview of CRCA models.

agg <i>L</i>	HR@3				
	non-truncated		truncated		
	max	\sum	max	\sum	
0	0.6062	0.5844	0.2031	0.2062	
3	0.6562	0.6406	0.3094	0.3094	
5	0.7250	0.7188	0.3312	0.3625	
7	0.8094	0.7469	0.4688	0.4906	
10	0.8187	0.8000	0.5437	0.5531	
11	-	-	0.6687	0.6625	
13	-	-	0.7031	0.7031	

The peak heuristic with a HR@3 value of 0.1406 is outperformed by all other variations. This was to be expected for truncated and non-truncated models with maximum lag $L > 0$. But even the truncated $L = 0$ model has a slight advantage over the heuristic, as the latter is not able to attribute a value to SOC and thus to detect the *soc loss* injection. In general the hit rate of the CRCA models is increasing with increasing L , indicating that delayed anomalies might get successively captured by models with higher maximum lag. Under the truncated models the summation aggregation leads to slightly better values compared to the maximum aggregation. The reverse is true for the non-truncated models. Surprisingly the non-truncated models outperform the truncated models with respect to HR@3. One reason is that the effective maximum lag is greater than L for non-truncated models as they can evaluate the dangling nodes that are otherwise truncated. The problem of the non-truncated structural model is the mechanism approximation at the

dangling nodes. It seems that in our particular case the dropping of parent dependencies at these nodes does still lead to good enough estimates, such that the benefit of additional lags outweighs the approximate nature of non-truncated models. Figure 7 visualizes the overall hit rate $HR@k$ comparing the truncated models with the peak heuristic (Figure 7a) and the truncated with the non-truncated models (Figure 7b). Figure 7b shows that only above maximum lag $L = 10$ the truncated models are in the range of the non-truncated.

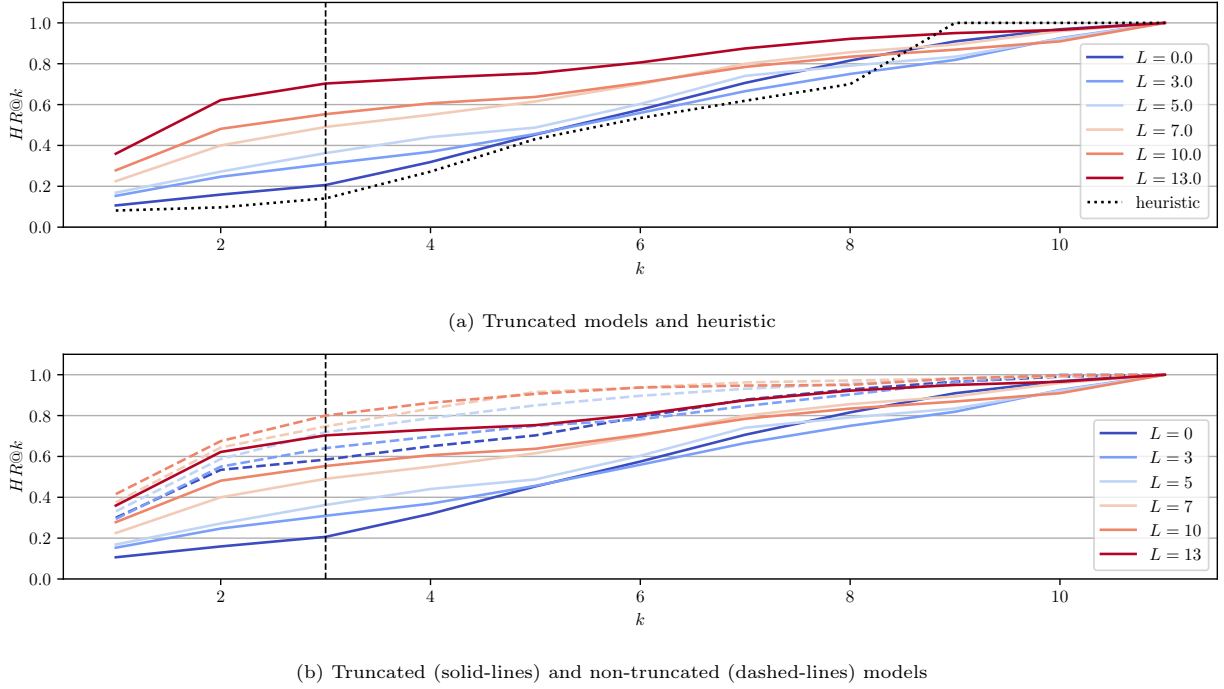


Figure 7: $HR@k$ values under Σ aggregation. The vertical dashed black line represents the $HR@3$ values.

Before investigating this effect in more detail we are going to evaluate the hit rate dependence on the maximum lag per injection. We can observe three basic patterns depending on the complexity of the injection:

1. Increasing with L

The hit rate increases substantially with an increase of the maximum lag L . These injection types are better captured by models with high maximum lag.

2. Little benefit of higher maximum lags L

The hit rate is on a high level independently of the maximum lag L . That is, there is no significant gain or loss switching from a model with low to a model with high maximum lag.

3. Non-beneficial / No pattern in L

While there are significant differences between the models with different L we can not observe a substantial increase of the hit rate with an increase of L .

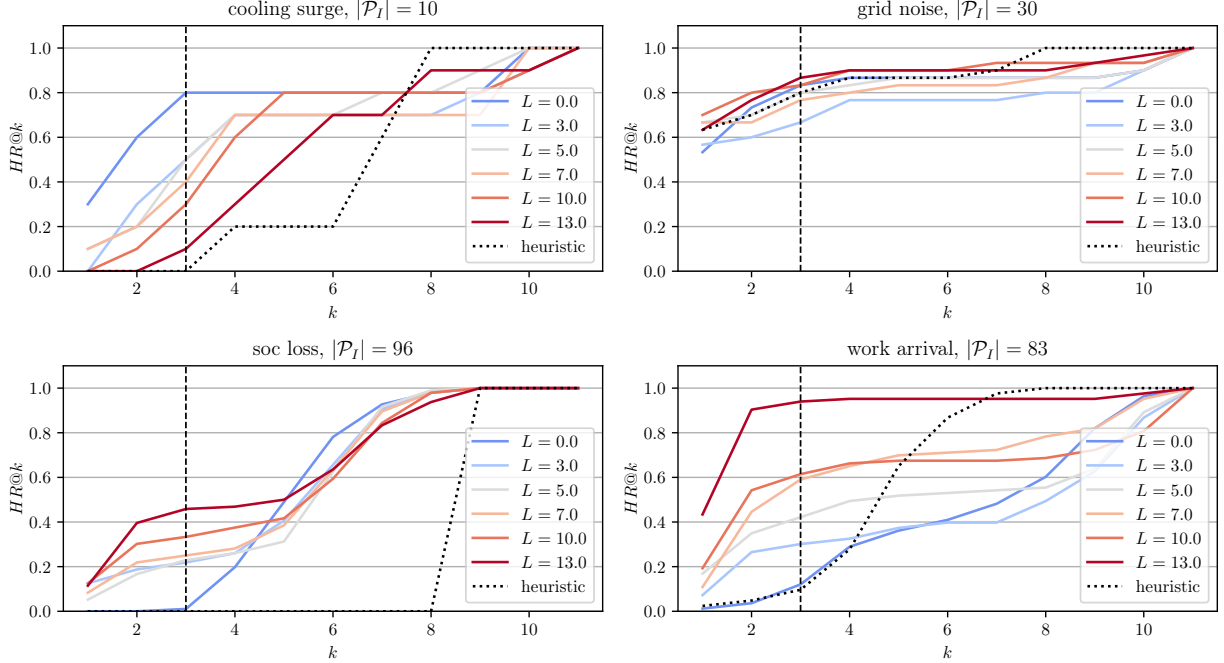


Figure 8: Hit rate $HR@k$ per injection under Σ aggregation of heuristic and truncated models: The hit rate of *soc loss* and *work arrival* injections increase with L (Category 1) while for *grid noise* there is little benefit in additional lags (Category 2). For *cooling surge* increasing lags seem non-beneficial (Category 3).

An overview of the different patterns that emerge using the truncated model is provided by Figure 8 and the full comparison of all injections can be found in Appendix A in Figure 14. For the truncated model we observe that the *temperature surge*, *work arrival*, *soc loss* and *bat fail* injections fall into the increasing category (Category 1). These injections target parts of the system that have a time delayed effect on the target node, which explains the observation. While the hit rate under the *soc loss* peaks increases too with L , the detection rate remains low. This not only lies in the long ranging effect of the injection, which is comparable to *work arrival*, but also in its indirect nature that prevents compensation of peaks. Also, the *bat fail* injection is increasing with L , except for individual lags (e.g. $L = 13$). Since its effect is rather immediate the differences between the different maximum lags are not as prominent. The low number of samples might also not allow the observation of a clear trend. Note that a disabled battery does not cause peaks by itself. It rather prevents peaks that would have been caused by other consumption nodes. The detection of *grid noise* and *cooling scale* peaks do not benefit from an increase in L (Category 2). The *grid noise* injection has an immediate effect on the target node and its structure is well aligned with the model structure. As we argued before this type of noise modification is an obvious change to be made in causal structural models. The injection produces immediate distinct peaks such that even the heuristic is able to outperform the truncated $L = 0$ model. In comparison, the *cooling scale* injection is more complex having a

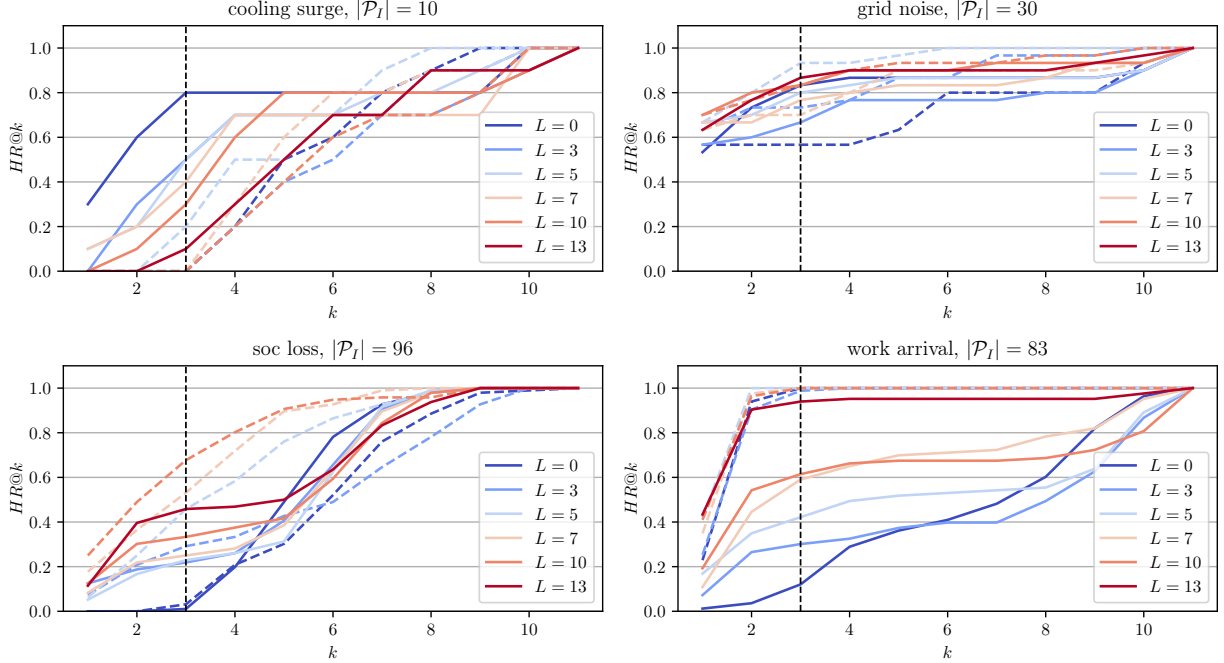


Figure 9: Hit rate $HR@k$ per injection under Σ aggregation of truncated (solid lines) and non-truncated models (dashed lines): The hit rate of *soc loss* remains increasing with L in the non-truncated case (Category 1) outperforming the truncated models given high enough L . As in the truncated case variations of L have only little effect on the already high hit rate of *grid noise* injections (Category 2). Both methods are on par in this case. While non-truncated models perform worse for *cooling surge* peaks (Category 3), they surpass the truncated models for *work arrival* injections maintaining a high hit rate independent of L (Category 2).

greater influence on the battery system potentially causing Grid peaks through delayed load cycles. The low performance of the peak heuristic can be explained through the constant factor affecting the CL increase during the injection time. Thus, there might hardly be any change in CL during the peak build up, leading the peak heuristic to assign a low attribution. The *cooling surge* injection falls into the remaining category (Category 3), as we observe a decreasing hit rate with increasing L . This observation might be a result of the low number of sample peaks. The injection design could provide another explanation. In contrast to *cooling scale* a fixed high consumption value is injected in CL. This is supposed to result in a difference compared to the baseline sample. However, in the observed time period this difference is rather subtle compared to the difference caused by the scale-up of *cooling scale*. This leads to peaks in which the CL node behaves less distinctive and thus to the difficulty to recover CL as the root cause.

We now investigate how the categorization changes in the non-truncated case. An overview is provided with Figure 9 and a full comparison can be found in Appendix A with Figure 15. For injections with time-delayed effects we see the most improvement compared to the truncated models. In particular for *soc loss*, *temp surge* and *work arrival* peaks the non-truncated models outperform the truncated. For the first two we observe an increase of the hit rate with increasing L as before (Category 1). *Work arrival* peaks

are even independently of L detected with high hit rate (Category 2). Only the $L = 13$ truncated model comes close to hit rates of the truncated models in case of *temperature surge* and *work arrival* injections. This observation is still present but not as distinct for *soc loss* peaks. For *grid noise* peaks we can see the same lag independent pattern as before (Category 2). With exception to $L = 0$ both methods achieve comparable results for this injection. In case of the *bat fail*, *cooling surge* and *cooling scale* injections we do not see distinct increases with L or a lag independent high hit rate (Category 3). While the non-truncated models performs worse for the cooling injections they yield a comparable hit rate performance for the *bat fail* injection. Again a higher number of peak samples may allow drawing different conclusions for *bat fail* and *cooling surge*. In general these observations support the hypothesis that the advantage of the non-truncated model is due to its higher effective lag.

As the hit rate comparison of truncated and non-truncated models with same maximum lag L is biased towards the non-truncated models in terms of attributable nodes we now compare both using their effective maximum lag. Given a node i we define the effective maximum lag $L_{\text{eff},i} := \max_i \mathcal{U}_i$ to be the maximum attributable lag of the node i . We then use L_{eff,c_I} to compare the two approaches on an injection basis with c_I being the node affected by the injection I . As can be seen in Figure 10 this partially explains the previous observed gap between both approaches. The closing of the gap between both approaches is most visual for the *temperature surge* injection, which is not surprising as the CL node has the highest number of time-lagged dependencies. Also for *work arrival* the truncated approach catches up more closely with increasing effective lag. One can also see that there remains a rather high gap in the *soc loss* case. We interpret the remaining gaps as follows: A better performance in one node also stabilizes the localization performance of the remaining features as the attributions sum to the IT-Score according to Equation 4. That is even if we compare the truncated and non-truncate approaches regarding *work arrival* peaks on basis of $L_{\text{eff},\text{TP}_a}$ the non-truncated model still might benefit from

$$L_{\text{eff},T} > L_{\text{eff},\text{TP}_a}$$

for the detection of anomalies in TP_a . For a comparison of all injections we refer to Figure 16 in Appendix A.

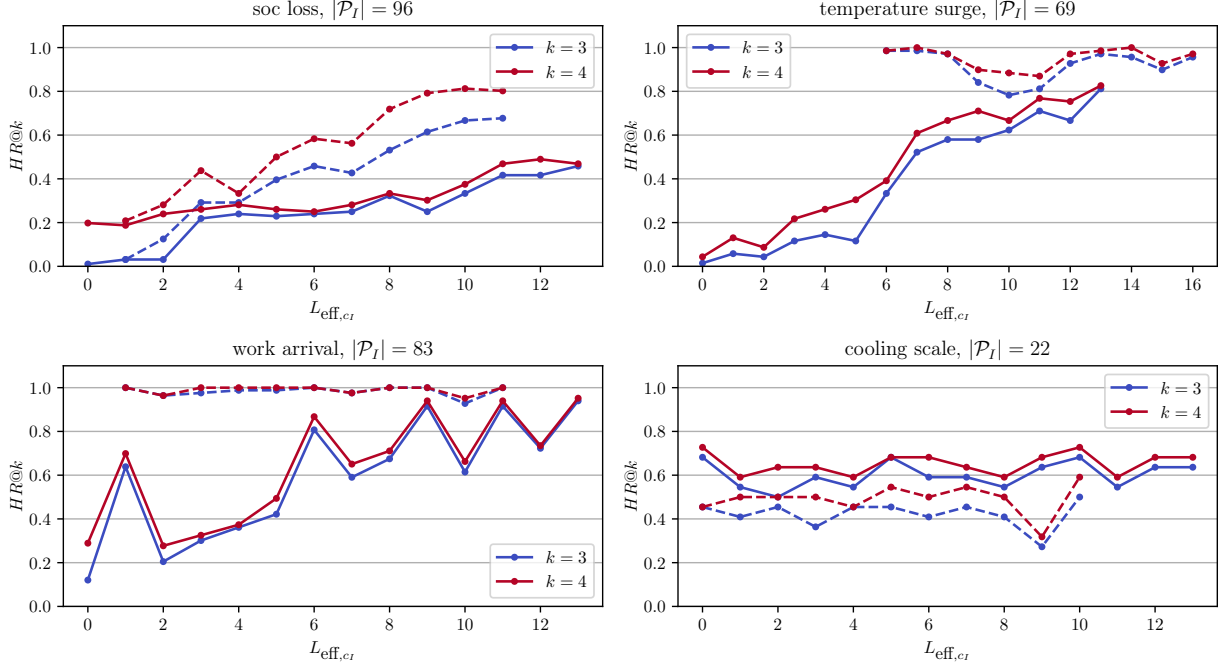


Figure 10: $HR@k$ under the Σ aggregation in dependence of the effective maximum lag $L_{\text{eff},ci}$ of the truncated (solid line) and non-truncated (dashed line) models.

4.2 Time Localization

In this section we evaluate the time localization capability in dependence of L for the truncated and non-truncated approaches. Table 3 provides an overview of the mean difference $d(t_I, \hat{t}_I)$ between actual and predicted injection time. Averages over all peaks are put in relation to averages over peaks within the range of the $L = 10$ models. The latter means that only peaks with a delay $\Delta_p := t_p - (t_I + \Delta_I)$ of less than 10 time steps are considered. Over all peaks and injections the mean difference decreases with L for the non-truncated models. Thereby the injection time \hat{t}_I is on average estimated too high, indicating that models with higher L might further improve the estimates. In the truncated case models with $L \leq 5$ seem to underestimate t_I (real injection time is after the predicted), resulting the lower average compared to the non-truncated. The truncated models start to improve with the inclusion of lags greater than six time steps. This hypothesis is backed by the corresponding averages for peaks with delay $\Delta_p \leq 10$. Under this restriction the averages for both, the truncated and the non-truncated models, are getting closer to a zero mean with higher L . Thereby truncated model exhibits a better average time localization behavior for $L \geq 7$. Note that after this threshold the feature location capability of the truncated models are also improving as they start to capture injections with time delay (see Figure 7a and 16). In particular only for $L > 6$ the truncated model can attribute to all the lagged temperature dependencies (see DGP in Figure 3). Further, the advantage of the non-truncated model for unrestricted Δ_p is not surprising given its additional

Table 3: Average difference $d(t_p, \hat{t}_p)$ of predicted and actual injection time per maximum lag L .

Δ_p	non-truncated		truncated		$d(t_p, \hat{t}_p)$	
	L	≤ 10	≤ 10	$< \infty$		
0		0.4779	-7.2059	5.9781	-1.1438	
3		0.1103	-2.7647	5.5187	1.9750	
5		0.1029	-0.6544	4.6688	3.1562	
7		0.0441	0.0294	3.9531	3.9875	
10		-0.3897	-0.2500	2.6344	3.2344	
13		-	-0.1765	-	3.0125	

attributable nodes. Figure 11 visualizes the difference distributions for the time delayed injections *soc loss*, *temperature surge* and *work arrival*. In general the time localization improves with higher maximum lag L decreasing the standard deviation.

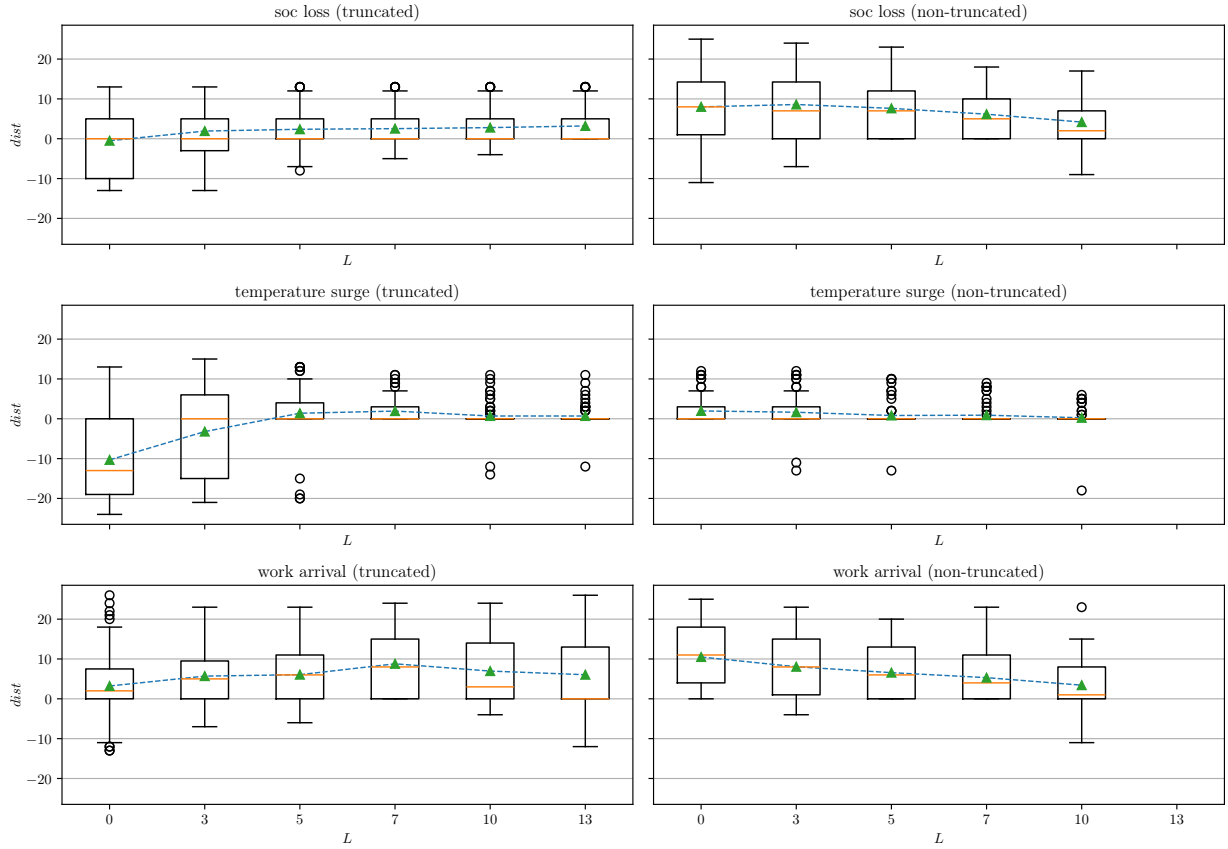


Figure 11: Box plots of differences $d(t_i, \hat{t}_i)$ among all peaks caused by delayed injections for truncated and non-truncated models. The mean difference is given by the dashed blue line.

For *temperature surge* under the truncated model this effect is the most striking and can be explained like before through the dependency structure of the DGP for $L \leq 7$. Note that the decrease also continues

for $L > 7$ as more injections fall into the model range. For the *work arrival* peaks we argue that the actual decrease only starts after the model is able to fully attribute to the temperature lags of the DGP. That is, for $L < 7$ we suspect that the model is more sensitive to work arrivals as it divides the IT-Score $S(x_t^n)$ among fewer nodes. These nodes do not capture the whole effect temperature has on cooling, while the contrary is true for the pronounced effect a high utilization has on the tool park consumption. For the more immediate injections the decrease in L is still present but not as pronounced (see Figure 17 in Appendix A). An observation that changes when restricting to peaks within reach of the $L = 10$ models as can be seen in Figure 18 in Appendix A. Note that the results of the *bat fail* and *cooling surge* injection in this regard are subject to a low sample size. By looking at the *soc loss* injection in 18 the difference between the truncated and non-truncated approach becomes clearly visible: the former lacks attributable lagged nodes which results in a systematic under estimation while the latter is prone to the mechanism miss specification at dangling nodes. Due to this the dangling nodes - which by definition have the highest lags in the model - may receive higher attributions resulting in the over estimation. In Section 4.3 we analyze this effect in greater detail.

We conclude that the truncated model requires L to be high enough to include all time lagged dependences of the mechanisms to correctly localize immediate anomalies - in our case $L = 7$. Adding further lags then pays in on to the localization of delayed anomalies.

4.3 Peak example

Lastly we investigate a specific peak caused by the *cooling surge* injection in greater detail. To inspect how the model approximation at the dangling nodes affects the prediction, we deliberately select a peak for which the non-truncated approach has difficulties. As shown in Figure 12 the nodes TP_b and CL are having a high power consumption contributing to the peak observed in the Grid node. The high tool park consumption is in line with the utilization UT_b , while the CL anomaly is due to the injection. The other nodes do not exhibit exceptional behavior. Since the peak occurs during the injection (in particular $t_I + 2 = t_p$) models with a low maximum lag should be able to detect the anomaly. When comparing the non-truncated $L = 1$ with the truncated $L = 2$ and $L = 7$ model we observe that the latter do rank cooling CL among the three highest root causes whereas the former does not (see Table 4). All models correctly attribute a high value to the tool park related nodes, but the non-truncated model wrongly attributes a high value to the temperature T .

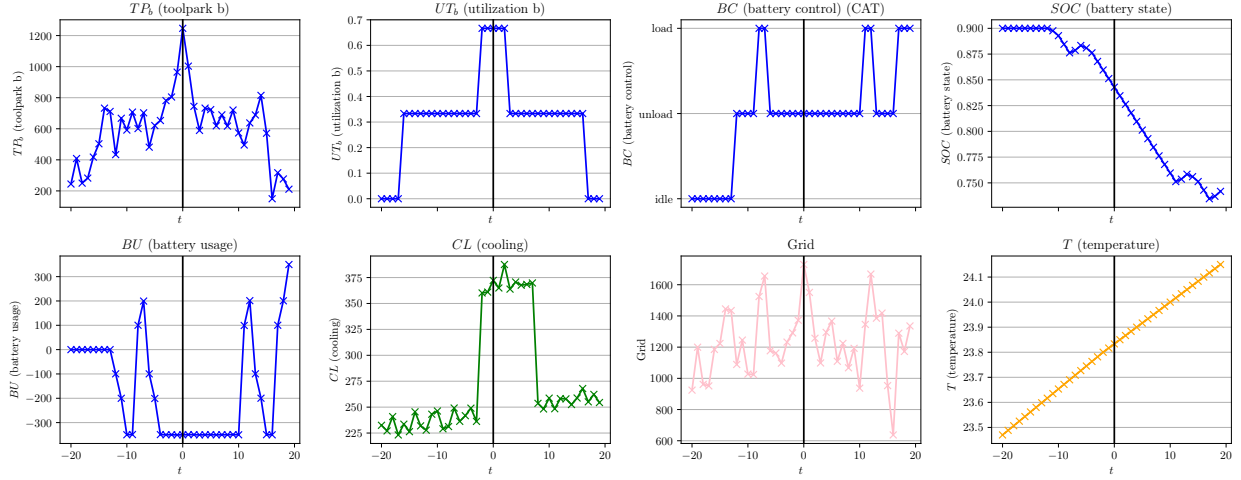


Figure 12: Example peak caused by the *cooling surge* injection: In addition to the injected cooling anomaly, the tool park TP_b has a consumption contributes to the peak in the Grid node. Node regarding the other tool park are omitted as they behave normal.

Table 4: Highest ranking root causes of truncated and non-truncated model under Σ lag aggregation for the example peak in Figure 12)

rank	L	non-truncated		truncated	
		1	2	2	7
1	TP _b	UT _b	UT _b	UT _b	UT _b
2	UT _b	CL	TP _b	TP _b	
3	T	TP _b	CL	CL	

By inspecting the time-lagged attributions we see high attribution values for $\phi_p(UT_b, 2)$, $\phi_p(TP_b, 2)$ and $\phi_p(T, 5)$ under the non-truncated $L = 1$ model (Figure 13a). These are compensated through lower attributions values at the Grid node and for $\phi_p(CL, 0)$ resulting in the detection failure. Comparing the non-truncated $L = 1$ model with the non-truncated $L = 2$ model we see that the attributions are shifted back assigning higher values at Grid and for $\phi_p(CL, 0)$, and lower values for $\phi_p(UT_b, 2)$, $\phi_p(TP_b, 2)$ and $\phi_p(T, 5)$. This causes the non-truncated model $L = 2$ model to identify the injected anomaly (see Table 4). However, the comparable truncated models attribute more steady and lower absolute values to the Grid, the T and TP_b nodes at $l \in \{2, 5\}$. This leads to more pronounced attributions for UT_b and CL . Investigating the noise distributions of the temperature N_{t-5}^T and tool park consumption $N_{t-2}^{TP_b}$ we see the reason for this: the distributions of the non-truncated $L = 2$ model have a longer tail as the corresponding functional model does not include all dependencies. This is shown in the Figures 13b and 13c. Due to this mechanism approximation the observed noise terms, depicted by the dashed orange line, are perceived as more exceptional and leading to higher attributions in contrast to models with intact mechanisms. Indeed, the tool park consumption distribution $N_{t-2}^{TP_b}$ of the non-truncated $L = 2$ and the truncated models does not

differ as the mechanism of the former is not misspecified. As this approximation effect can not be isolated,

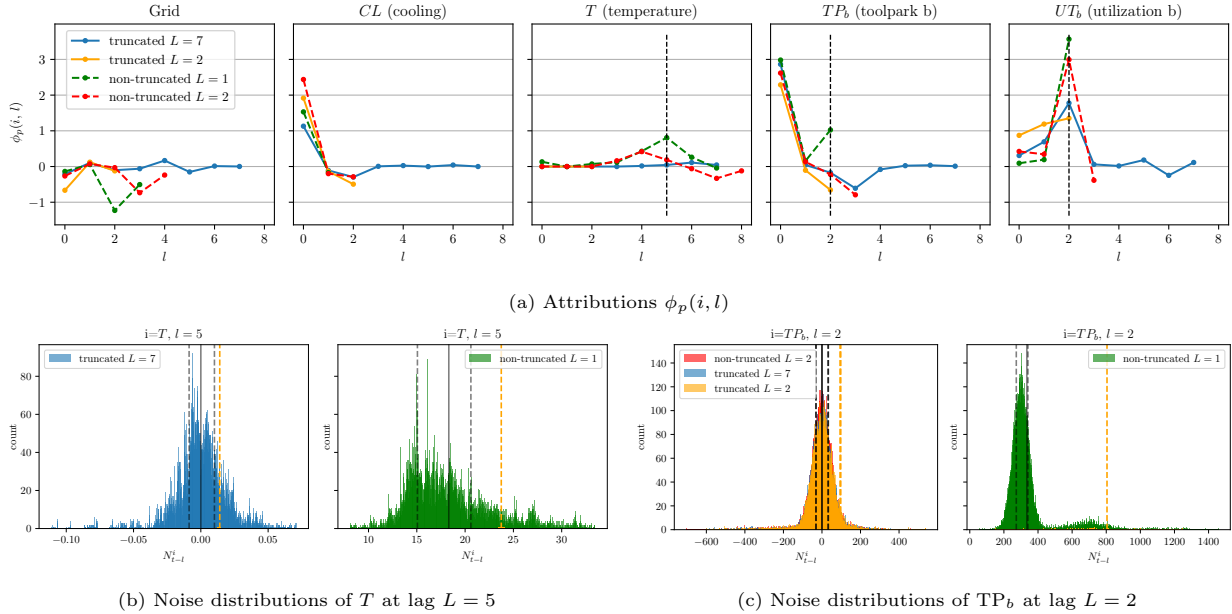


Figure 13: Time dependent attributions and noise distributions for the example peak from Figure 12: The divergent attributions of the truncated and non-truncated models at $l = 2$ for TP_b and at $l = 5$ for T (Figure 13a) are related to the noise distributions of the models (Figures 13b and 13c): The orange vertical dashed lines in the distribution figures signify the observed noise values of the peak at the corresponding time-lagged node. The $q_{0.25}$ and $q_{0.75}$ quantiles are given by black vertical dashed lines. In the long-tailed distributions of the non-truncated $L = 1$ model the observed noises are perceived as exceptional. This stays in contrast to distributions of the same nodes for the other models and explains the high attributions of the non-truncated $L = 1$ model.

we conclude that it is important to keep all attributable mechanisms intact.

5 Conclusion

In this paper we adapted the CRCA method of Budhathoki et al. [2022] to time dependent systems. Our method can be interpreted as an extension of the causal formalization of the term “root-cause” given by Budhathoki et al. [2022] to time-lagged systems.

We studied two methods that transform the infinite dependency graph of time-dependent systems into a finite one, a property required to apply CRCA. The truncation approach ensures that the causal mechanisms of all nodes up to a maximum time-lag are left intact by conditioning on direct parent dependencies that exceed this maximum. While this is the obvious thing to do from a causal perspective, it limits the model range to exactly this maximum lag. The non-truncation approach approximates the mechanism of the nodes conditioned by removing their dependencies. This results in a higher number of attributable nodes and thus potentially to a higher time range at the sacrifice of a causally correct model specification. We benchmarked both approaches using a DGP related to energy management in manufacturing systems. The DGP is memory

afflicted, has a control mechanism that affects the system target, and exhibits instantaneous and time-delayed effects. All these properties make it challenging to recover root-causes. Moreover, we argue that our work provides a blueprint for an application of the CRCA method in energy systems in order to explain peaks in the power consumption peaks.

Our results show that the CRCA adaption is able to recover injected root-causes with different delays broadening the scope of CRCA. Surprisingly, the non-truncation outperforms the truncation approach in the feature localization, whereas for time-localization the latter performs more stable for causes in the range of the model. Our analysis indicates that truncation prevents an over attribution at the start nodes, at the same time limiting the model range. That is, it prevents that wrong nodes get a high attribution at the expense of the actual root-cause being out of the model range. In our particular case this effect seems to payoff in favor of the non-truncated model. Nevertheless, this might not be a general tendency as the dependency structure of the investigated system might be more prone to confounding, and thus invalidating the approximations made in the non-truncation case even more. In case of the truncation approach we argue that at least all time lagged dependencies of the mechanisms should be attributable to consistently recover instantaneous root-causes. Every further lag then expands the actual model range.

Like for the time independent CRCA method the downside of the methodology is the required computational effort to evaluate the Shapley values. Under the given independence assumptions an efficient implementation can limit the memory complexity to the non-time dependent case and at least reduce the computational complexity for the noise sampling and model estimation but not for the Shapley symmetrization. The necessary computational improvement of the method is still subject to further research. Some recent approaches try to improve the method in case of distinct singular root-causes Okati et al. [2024], a scenario that we deem unrealistic for controlled systems. In the time-dependent domain recurrent approaches, e.g. a LSTM like causal automata that scans the time series and produces consequent attributions based on its own memory could be a promising future research direction in this regard. Moreover, in our specific application scenario we asked of which causes had lead to the emergence of a peak in the energy consumption. To be precise, we only gave answer to half of it. Namely, which factors had contributed to a high consumption. But the nature of the peak is one that has a symmetry requiring to also ask: what were the factors that had led to a decline after the peaks maximum? As this “going back to normal” can also be regarded as an outlier event the same methodology might be used to give an answer to this. While we focused to benchmark a single method on a challenging DGP, further research should also benchmark the pure causal CRCA approach against the time-dependent granger causality approaches.

A Additional Results

In the following we present additional results of the feature and time localization capability of the truncated and non-truncated models. These complement the results shown in Section 4.

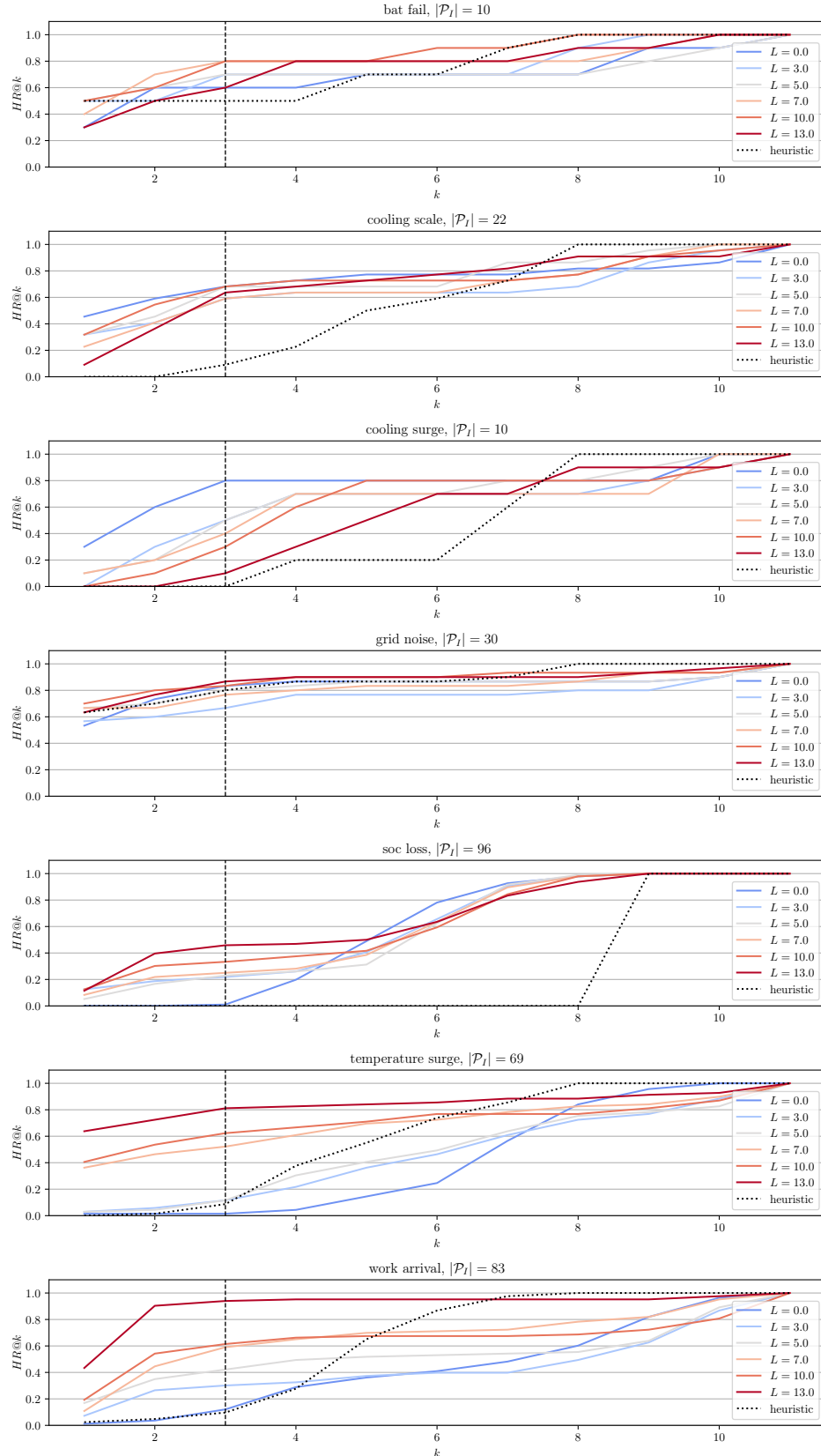


Figure 14: Hit rate $HR@k$ for all injections under Σ aggregation of heuristic and truncated models.

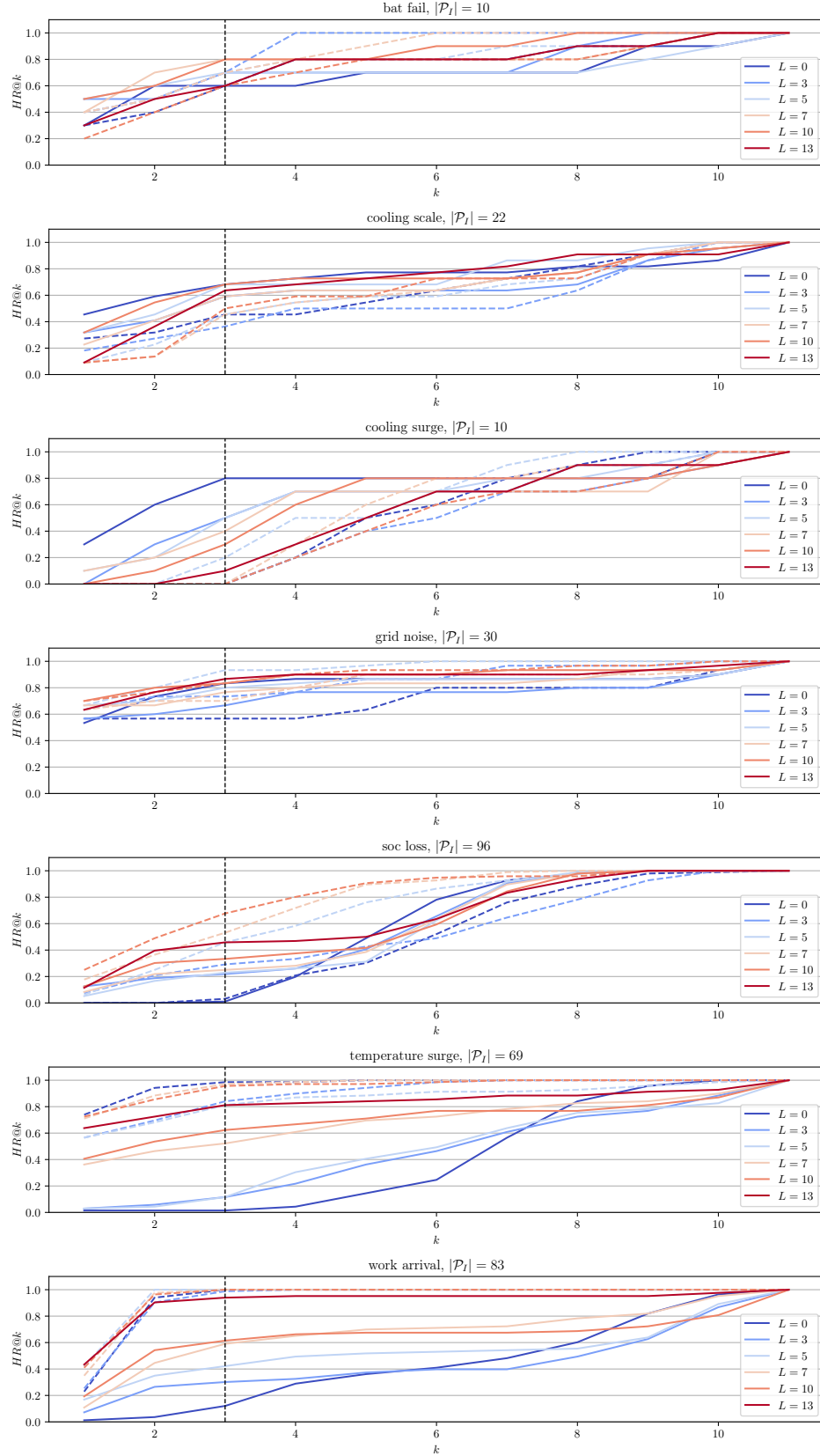


Figure 15: Hit rate $HR@k$ for all injections under Σ aggregation of truncated (solid lines) and non-truncated models (dashed lines).

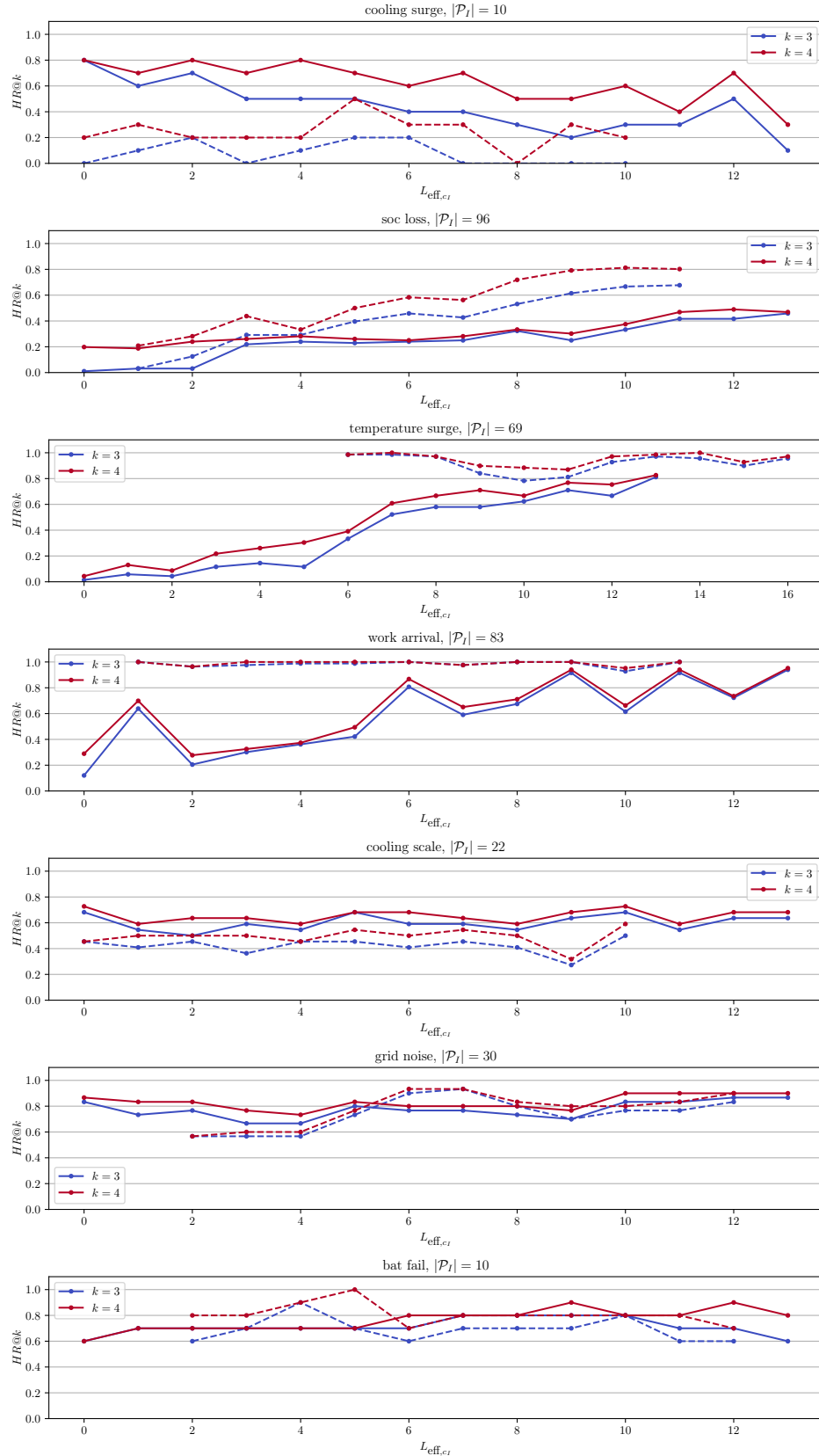


Figure 16: $HR@k$ for all injections under the Σ aggregation in dependence of the effective maximum lag $L_{\text{eff},ci}$ of the truncated (solid line) and non-truncated (dashed line) models.

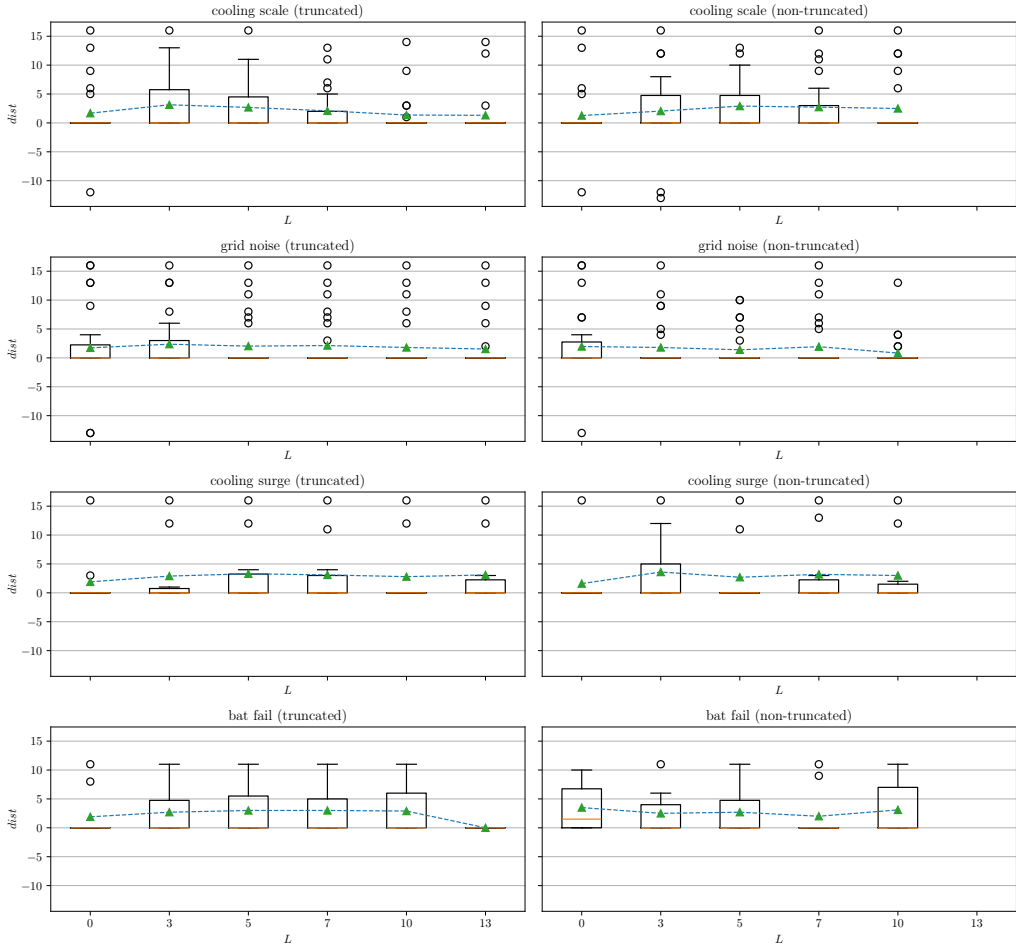


Figure 17: Box plots of the difference $d(t_i, \hat{t}_i)$ among all peaks caused by immediate injections for truncated and non-truncated models. The mean difference is given by the dashed blue line.

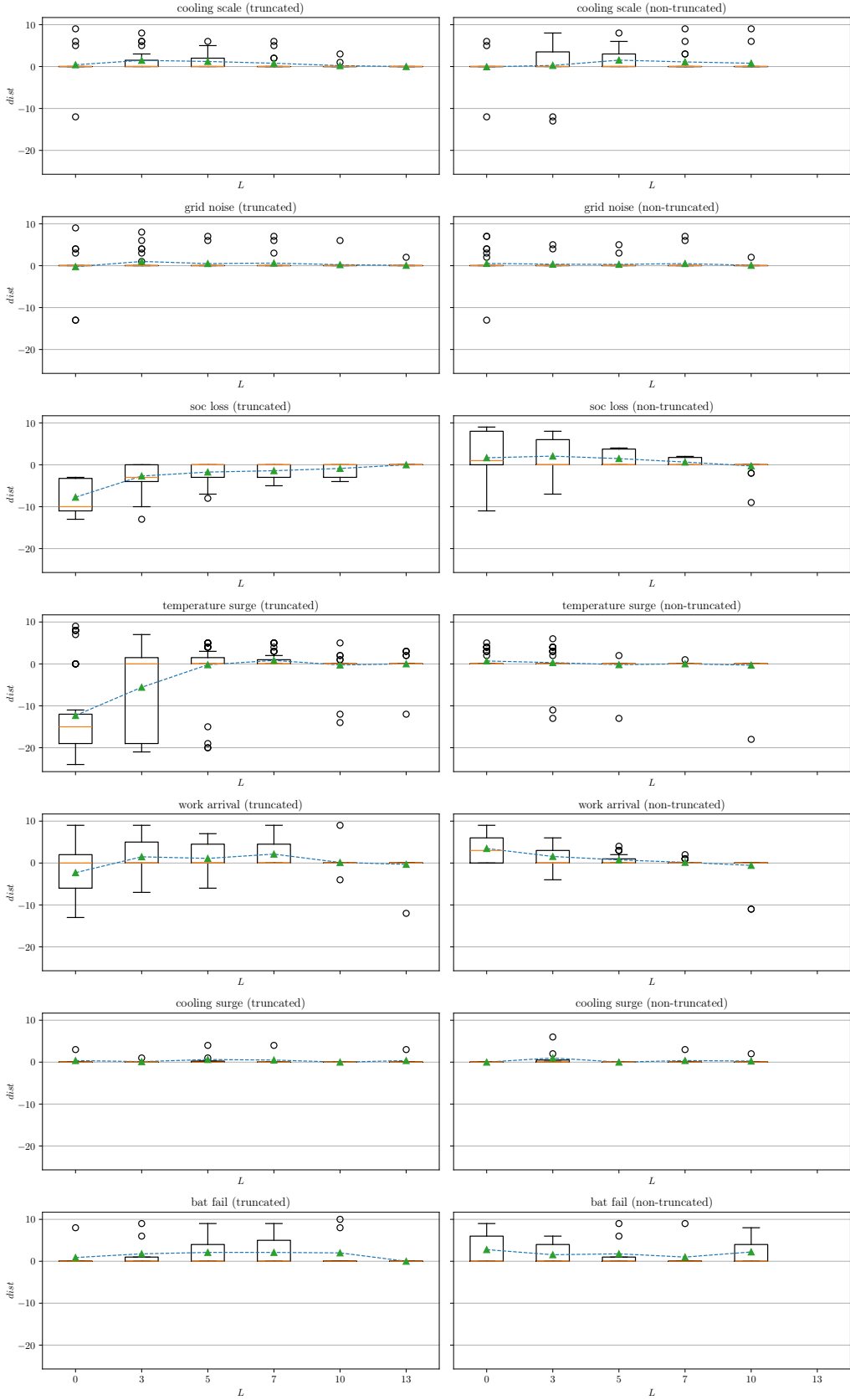


Figure 18: Box plots of the difference $d(t_i, \hat{t}_i)$ among all peaks with $\Delta_p \leq 10$ for truncated and non-truncated models. The mean difference is given by the dashed blue line.

Acknowledgements

This work was funded by the Bavarian Joint Research Program (BayVFP) – Digitization (Funding reference: DIK0294/01). The research partners AMS-Osram and Economic AI kindly thank the VDI/VDE-IT Munich for the organization and the Free State of Bavaria for the financial support.

References

Patrick Blöbaum, Peter Götz, Kailash Budhathoki, Atalanti A. Mastakouri, and Dominik Janzing. Dowhy-gcm: An extension of dowhy for causal inference in graphical causal models. *Journal of Machine Learning Research*, 25(147):1–7, 2024. URL <http://jmlr.org/papers/v25/22-1258.html>.

Dérick G. F. Borges, Eluã R. Coutinho, Thiago Cerqueira-Silva, Malú Grave, Adriano O. Vasconcelos, Luiz Landau, Alvaro L. G. A. Coutinho, Pablo Ivan P. Ramos, Manoel Barral-Netto, Suan T. R. Pinho, Marcos E. Barreto, and Roberto F. S. Andrade. Combining machine learning and dynamic system techniques to early detection of respiratory outbreaks in routinely collected primary healthcare records. *BMC Medical Research Methodology*, 25(1), April 2025. ISSN 1471-2288. doi: 10.1186/s12874-025-02542-0.

Kailash Budhathoki, Lenon Minorics, Patrick Bloebaum, and Dominik Janzing. Causal structure-based root cause analysis of outliers. In Kamalika Chaudhuri, Stefanie Jegelka, Le Song, Csaba Szepesvari, Gang Niu, and Sivan Sabato, editors, *Proceedings of the 39th International Conference on Machine Learning*, volume 162 of *Proceedings of Machine Learning Research*, pages 2357–2369. PMLR, 17–23 Jul 2022. URL <https://proceedings.mlr.press/v162/budhathoki22a.html>.

Ahmed Dawoud and Shravan Talupula. Prorca: A causal python package for actionable root cause analysis in real-world business scenarios. March 2025. doi: 10.48550/ARXIV.2503.01475.

Yixiu Guo, Yong Li, Sisi Zhou, Zhenyu Zhang, Yahui Wang, Yong Xu, Xusheng Yang, Zuyi Li, and Mohammad Shahidehpour. Optimal dispatch for integrated energy system considering data-driven dynamic energy hubs and thermal dynamics of pipeline networks. *IEEE Transactions on Smart Grid*, 15(5):4537–4549, September 2024. ISSN 1949-3061. doi: 10.1109/tsg.2024.3382740.

Azam Ikram, Sarthak Chakraborty, Subrata Mitra, Shiv Saini, Saurabh Bagchi, and Murat Kocaoglu. Root cause analysis of failures in microservices through causal discovery. 35:31158–31170, 2022. URL https://proceedings.neurips.cc/paper_files/paper/2022/file/c9fc02e6445c7dfbad6986abee53d0d-Paper-Conference.pdf.

Cheng-Ming Lin, Ching Chang, Wei-Yao Wang, Kuang-Da Wang, and Wen-Chih Peng. Root cause analysis in microservice using neural granger causal discovery. February 2024. doi: 10.48550/ARXIV.2402.01140.

Dewei Liu, Chuan He, Xin Peng, Fan Lin, Chenxi Zhang, Shengfang Gong, Ziang Li, Jiayu Ou, and Zheshun Wu. Microhecl: High-efficient root cause localization in large-scale microservice systems. pages 338–347, May 2021. doi: 10.1109/icse-seip52600.2021.00043.

Nastaran Okati, Sergio Hernan Garrido Mejia, William Roy Orchard, Patrick Blöbaum, and Dominik Janzing. Root cause analysis of outliers with missing structural knowledge. June 2024. doi: 10.48550/ARXIV.2406.05014.

Judea Pearl. *Causality*. Cambridge University Press, Cambridge, second edition, reprinted with corrections edition, 2022. ISBN 9780521895606. Hier auch später erschienene, unveränderte Nachdrucke.

Jonas Peters. *Elements of causal inference*. The MIT Press, Cambridge, Massachusetts, 2017. ISBN 9780262037310.

J. Runge. Causal network reconstruction from time series: From theoretical assumptions to practical estimation. *Chaos: An Interdisciplinary Journal of Nonlinear Science*, 28(7), July 2018. ISSN 1089-7682. doi: 10.1063/1.5025050.

Jakob Runge, Sebastian Bathiany, Erik Bollt, Gustau Camps-Valls, Dim Coumou, Ethan Deyle, Clark Glymour, Marlene Kretschmer, Miguel D. Mahecha, Jordi Muñoz-Marí, Egbert H. van Nes, Jonas Peters, Rick Quax, Markus Reichstein, Marten Scheffer, Bernhard Schölkopf, Peter Spirtes, George Sugihara, Jie Sun, Kun Zhang, and Jakob Zscheischler. Inferring causation from time series in earth system sciences. *Nature Communications*, 10(1), jun 2019a. doi: 10.1038/s41467-019-10105-3.

Jakob Runge, Peer Nowack, Marlene Kretschmer, Seth Flaxman, and Dino Sejdinovic. Detecting and quantifying causal associations in large nonlinear time series datasets. *Science Advances*, 5(11), nov 2019b. doi: 10.1126/sciadv.aau4996.

Lloyd S. Shapley. *A Value for N-Person Games*. RAND Corporation, Santa Monica, CA, 1952. doi: 10.7249/P0295.

Amit Sharma and Emre Kiciman. Dowhy: An end-to-end library for causal inference. November 2020. doi: 10.48550/ARXIV.2011.04216.

Eric V. Strobl. Counterfactual formulation of patient-specific root causes of disease. *Journal of Biomedical Informatics*, 150:104585, February 2024. ISSN 1532-0464. doi: 10.1016/j.jbi.2024.104585.

Dongjie Wang, Zhengzhang Chen, Jingchao Ni, Liang Tong, Zheng Wang, Yanjie Fu, and Haifeng Chen.
Hierarchical graph neural networks for causal discovery and root cause localization. February 2023. doi:
10.48550/ARXIV.2302.01987.